

# PCCP

Accepted Manuscript



This is an *Accepted Manuscript*, which has been through the Royal Society of Chemistry peer review process and has been accepted for publication.

*Accepted Manuscripts* are published online shortly after acceptance, before technical editing, formatting and proof reading. Using this free service, authors can make their results available to the community, in citable form, before we publish the edited article. We will replace this *Accepted Manuscript* with the edited and formatted *Advance Article* as soon as it is available.

You can find more information about *Accepted Manuscripts* in the [Information for Authors](#).

Please note that technical editing may introduce minor changes to the text and/or graphics, which may alter content. The journal's standard [Terms & Conditions](#) and the [Ethical guidelines](#) still apply. In no event shall the Royal Society of Chemistry be held responsible for any errors or omissions in this *Accepted Manuscript* or any consequences arising from the use of any information it contains.



Journal Name

ARTICLE TYPE

Cite this: DOI: 10.1039/xxxxxxxxxx

## Phase changes of the water hexamer and octamer in the gas phase and adsorbed on polycyclic aromatic hydrocarbons †

Luiz Fernando L. Oliveira,<sup>a</sup> Jérôme Cuny,<sup>\*a</sup> Maxime Morinière,<sup>b</sup> Léo Dontot,<sup>a</sup> Aude Simon,<sup>a</sup> Fernand Spiegelman<sup>a</sup> and Mathias Rapacioli<sup>\*a</sup>

Received Date  
Accepted Date

DOI: 10.1039/xxxxxxxxxx

www.rsc.org/journalname

We investigate thermodynamic properties of small water clusters adsorbed on polycyclic aromatic hydrocarbons (PAHs), which are relevant systems in the context of astrophysical and atmospheric chemistry. We present heat capacity curves computed from parallel-tempering molecular dynamics and Monte Carlo simulations that were performed using the self-consistent-charge density-functional based tight-binding method. These curves are characteristic of the phase changes occurring in the aggregates and provide useful information on the evolution of the interaction between the water molecules and the PAHs as a function of temperature. After benchmarking our approach on the water hexamer and octamer in the gas phase, we present some results for these same clusters adsorbed on coronene and circumcoronene. When compared to the curves obtained for the isolated water clusters, the phase change temperature significantly decreases for the (H<sub>2</sub>O)<sub>8</sub>-PAH clusters whereas it depends on the nature of the PAH in the case of the hexamer. We analyse these differences as connected to the relative energies of the optimized characteristic isomers and to their dynamical behavior. We also evidence the population changes of the various cluster isomers as a function of the temperature.

### 1 Introduction

Polycyclic aromatic hydrocarbons (PAHs) have been proposed as the carriers of the so-called interstellar aromatic infrared bands (AIBs)<sup>1,2</sup> and it has also been suggested that the PAH population would contain ~20% of the interstellar carbon.<sup>3,4</sup> Many experimental and theoretical studies have been performed to prove these assumptions. In particular, it was shown that the interaction of PAHs with atoms of astrophysical relevance such as iron and silicon had an influence on the positions and intensities of the AIBs.<sup>5–10</sup> A second example illustrating the importance of PAHs in the field of astrochemistry is their potential catalytic role in the formation of H<sub>2</sub>.<sup>11,12</sup> Indeed, the formation of molecular hydro-

gen may occur in regions of the interstellar medium where the UV flux is low and the concentration of H is high. Under such conditions, the presence of PAHs has been shown to energetically favour the formation of H<sub>2</sub>.<sup>12–14</sup>

PAHs are also formed by the human use of fossil fuels,<sup>15,16</sup> as well as by natural processes which make them atmospherically abundant molecules. As the atmosphere contains a high concentration of water molecules, their interaction with PAHs is of primary interest since PAHs maybe responsible for various health problems, as for instance several types of cancer.<sup>17–19</sup> This has thus motivated growing investigations of their properties in both environmental and atmospheric science.<sup>15,20–24</sup> Lastly, although presenting finite size effects, water-PAH clusters can be viewed as model systems in the studies of the interaction of water molecules with carbonaceous surfaces that are relevant systems for several applications, such as sensors,<sup>25</sup> electrochemical devices,<sup>26</sup> nanofluidics,<sup>27</sup> electrochemistry<sup>28</sup> and water desalination.<sup>29</sup>

Water clusters in the gas phase have received a considerable attention as they represent prototype systems to further untangle the complex structural and dynamical properties of liquid water.<sup>30,31</sup> Thus, water clusters have been the focus of numerous experimental and theoretical studies. In particular, a significant

† Electronic Supplementary Information (ESI) contain additional pictures to illustrate the convergence of the heat capacity curves with the length of the simulation, the effect of the choice of the DFTB Mulliken or CM3 charges, as well as the effect of freezing the PAH intramolecular degrees of freedom. Molecular representation of the characteristic cluster structures discussed in the article are also provided.

<sup>a</sup> Laboratoire de Chimie et Physique Quantiques LCPQ/IRSAMC, Université de Toulouse (UPS) and CNRS, 118 Route de Narbonne, F-31062 Toulouse, France. Fax: +33 (0)5 61 55 60 65 ; Tel: +33 (0)5 61 55 68 34

<sup>b</sup> Laboratoire de simulation atomistique (LSim), Univ. Grenoble Alpes, INAC-SP2M, F-38000 Grenoble, France and CEA, INAC-SP2M, F-38000 Grenoble, France.

contributions may be attributed to the global optimization community as highlighted by the vast literature on the subject.<sup>32–37</sup> Among all these studies, the water hexamer has deserved a particular attention as it represents the transition between planar and three-dimensional structures.<sup>38–51</sup> This cluster has been a subject of a long term debate as two structures; namely the *cage* and the *prism*, were proposed to compete for being the lowest energy isomer. On the one hand, theoretical studies performed using methods of various levels of accuracy have led to opposite conclusions.<sup>41,42,44–47,51</sup> On the other hand, experimental studies have recently concluded that the *cage* structure is the lowest energy isomer although it seems to coexist with other structures even at very low temperatures.<sup>38–40,48,50</sup> Another intensively studied water cluster is the water octamer for which the lowest energy structure is a *cube* as reported by both theoretical<sup>52–58</sup> and experimental<sup>59,60</sup> studies.

Among the theoretical works dealing with water clusters in the gas phase and adsorbed on carbonaceous surfaces, thermodynamical properties have often been studied through the computation of heat capacity curves.<sup>61–67</sup> Indeed, it is a convenient quantity that allows for an easy identification of the temperature at which a phase change occurs. The determination of that temperature is of paramount importance as it is characteristic of both the strength of the intermolecular interactions in the aggregate and its thermal stability.

Computation of finite temperature properties usually requires long simulation times to reach thermal equilibrium and to achieve statistical convergence. Typically, millions of single-point energy calculations are required, which is a bottleneck for *ab initio* potentials. For this reason, most of the aforementioned studies have been performed using force field (FF) potentials.<sup>61–63,66,67</sup> In particular, Pedulla and Jordan rationalized the influence of the choice of the FF on the simulated heat capacity curves of the water hexamer and octamer.<sup>61</sup> They tested a number of FF among which polarizable and rigid body ones: TIP3P,<sup>68</sup> TIP4P,<sup>69</sup> SPC/E,<sup>70</sup> MCY,<sup>71</sup> CKL,<sup>72</sup> NCC,<sup>73</sup> RPOL,<sup>74</sup> DC<sup>75</sup> and BDKL.<sup>76</sup> They observed a variation of ~100 K and ~200 K in the phase change temperature of (H<sub>2</sub>O)<sub>6</sub> and (H<sub>2</sub>O)<sub>8</sub>, respectively, with respect to the nature of the FFs. Douady *et al.* further performed a similar study on the (H<sub>2</sub>O)<sub>20</sub> cluster and found a variation of ~20 K of the phase change temperature for the different tested FF.<sup>63</sup> Thermodynamic properties of water clusters interacting with carbon-based materials have also been addressed.<sup>66,67</sup> As for water clusters, FF potentials were also used in those investigations. Among other results, they showed that the interaction with various carbonaceous cations results in a significant decrease of the melting temperature of the water octamer.

Even though the aforementioned studies present considerable achievements in the description of phase changes in water clusters, both isolated and adsorbed on carbonaceous species, the spread of the results obtained using different FF is disappointing. There is thus a need to go beyond FF schemes while maintaining a reasonable computational cost. A possible solution is to use a parametrised method that provides an explicit quantum description of the electronic structure. One example of such a method is the self-consistent-charge density-functional based tight-binding

(SCC-DFTB) method.<sup>77–80</sup> This approach has already been shown to provide a good description of the intermolecular interactions governing the physics of molecular clusters, in particular PAH clusters,<sup>81–84</sup> water clusters,<sup>64,85–88</sup> and water clusters adsorbed on a PAH.<sup>85–87</sup> However, to the best of our knowledge, the SCC-DFTB method has only been used once to study the heat capacity of water clusters.<sup>64</sup> This study focused on the water octamer and showed that the SCC-DFTB approach leads to results similar to those obtained with the DC potential. However, no further work using the SCC-DFTB approach has been performed on water clusters adsorbed on surfaces. Thus, to fill this gap, we present heat capacity curves calculated for the (H<sub>2</sub>O)<sub>6</sub> and (H<sub>2</sub>O)<sub>8</sub> clusters, both isolated and adsorbed on two PAH molecules, namely coronene (C<sub>24</sub>H<sub>12</sub>) and circumcoronene (C<sub>54</sub>H<sub>18</sub>). These systems were chosen as they can be regarded as prototype examples of a water-carbonaceous system.

This paper is structured as follows: the next section describes the strategy followed to simulate heat capacity curves, the SCC-DFTB method used, the parallel-tempering molecular dynamics (MDPT) and Monte-Carlo (MCPT) techniques employed to explore the PESs. Section 3 provides the main results of our investigations. We discuss the differences in the heat capacity curves for the water clusters isolated and adsorbed on the PAHs. These differences are also discussed in terms of the temperature dependence of the isomer populations. Finally, conclusions and possible developments are presented in the last section.

## 2 Methodology

**Computation of the Heat Capacity Curves.** The simulation of a heat capacity curve as a function of the temperature can be achieved in different ways. The simplest one consists in performing MC or MD simulations at different temperatures and extracting for each one the heat capacity from a direct calculation of the variance of the potential energy. This approach is somewhat statistically inefficient and thus alternative approaches have been proposed. Indeed, to reduce the statistical noise and to extrapolate heat capacities at temperatures not explicitly simulated, one can benefit from the fact that in MD or MC simulations a given configuration may be visited at different temperatures. Labastie and Whetten,<sup>89</sup> as well as Ferrenberg and Swendsen,<sup>90</sup> and Bichara *et al.*<sup>91</sup> have independently proposed similar methods taking advantage of these overlaps to calculate heat capacity curves. In the present work, we have used the former one which we will refer to as the multiple histogram method. It uses probability densities of finding an energy at a given temperature leading to a set of histograms for each simulated temperature. Thermodynamical quantities, such as entropy or normalized density of states are further obtained from a least square minimization process. The heat capacity is then determined from the following formula:

$$C(T) = \frac{3Nk_B}{2} + \frac{\langle V^2 \rangle - \langle V \rangle^2}{k_B T^2}, \quad (1)$$

where  $T$  is the temperature and  $V$  the potential energy. This latter is computed from the density of states, the entropy and the partition function obtained from the multiple histogram scheme

that is described in details in Supplementary Information. The first term of equation 1 is the classical limit of the heat capacity at  $T = 0$  K. We decided not to include this term as it simply corresponds to a global shift of the curves, making less convenient the direct comparison between rigid and non-rigid body calculations. It is also worth pointing out that nuclear quantum effects are expected to have a significant impact on this quantity at low temperature making its classical evaluation not relevant.

**Populations of Isomers.** In order to draw a link between a heat capacity curve and the structural modifications occurring in the aggregate, we have evaluated the relative populations of the cluster isomers as functions of temperature. The identification of various isomers inevitably contains a degree of arbitrariness. In the present work, we choose to discriminate them counting the number of oxygen-oxygen rings that exist in a given configuration and to relate this number to previously identified characteristic structures. To do so, we chose a O-O distance cutoff of 3.25 Å to define bounded water molecules and we applied the algorithm proposed by Yuan and Cormack.<sup>92</sup> Thus, in the text, each water cluster is identified by a series of integers in brackets corresponding to the number of cycles it contains, ranging from 3 to 6 for the water hexamer and from 3 to 8 for the water octamer. For instance, [2100] corresponds to a water hexamer containing two three-membered rings and one four-membered ring.

**Computation of the PES.** We used the SCC-DFTB method, an approximated density functional theory (DFT) scheme whose computational efficiency relies on the use of a minimal valence basis-set and parametrised integrals. In the present work, we used the mio-set for Slater-Koster tables.<sup>80</sup> The SCC-DFTB approach requires additional corrections to properly deal with weak intermolecular interactions.<sup>83</sup> To do so, we used an empirical dispersion term<sup>93</sup> and a correction for the Coulomb interaction in which the Mulliken charges are replaced by the Class IV - Charge Model 3 developed in the context of DFT<sup>94,95</sup> and later introduced in the SCC-DFTB potential.<sup>96</sup> In previous studies, we have already demonstrated the importance of including such terms to accurately describe water and water-PAH aggregates.<sup>85-87</sup> In all our calculations, the self-consistent process is stopped when the largest atomic charge fluctuation is smaller than  $10^{-8}$  a.u.

**Exploration of the PES.** In order to extract structural and thermodynamical properties, an extensive exploration of the PES is required. In this work, this has mainly been achieved using MDPT simulations.<sup>97,98</sup> For the water-PAH clusters, it appears that a proper convergence of the heat capacity curves is much more easily achieved when freezing the intramolecular modes of the PAH. Thus, all the results presented and discussed in this article have been performed doing so. Some results obtained without freezing the intramolecular modes of the PAH are presented and discussed in section 3 of the Supp. Info. To prove that our results do not suffer from any convergence insufficiency and are reproducible irrespective to the approach used to explore the PES, we additionally performed simulations based on the MCPT technique on the two bare water clusters.<sup>99,100</sup>

In the parallel-tempering algorithm, we used 32, 40 and 60 temperatures for the bare water clusters, the  $(\text{H}_2\text{O})_6$ -PAH and the  $(\text{H}_2\text{O})_8$ -PAH aggregates, respectively. We used a linear dis-

tribution of the temperatures ranging from 10 K to 240 K for the hexamer-containing aggregates and from 10 K to 400 K for the octamer-containing aggregates. We used a timestep of 0.1 fs to integrate the equations of motion in the MDPT simulations. The test to perform the PT exchanges was done each 1000 MD steps. For the simulation of the heat capacity curves, we removed from our analysis the 25 MD steps following the PT exchange to account for the thermalisation of the system. As the MDPT simulations are performed in the canonical ensemble, the choice of the thermostat is a crucial point. Gamboa *et al.*<sup>101</sup> have shown that for the calculation of heat capacity curves, the Nosé-Hoover chain thermostat,<sup>102-104</sup> is over-performing other thermostating schemes such as the velocity re-scaling, the Berendsen and the isokinetic thermostats. Therefore, we used the Nosé-Hoover chain thermostat for all the simulations performed in this study. The thermostat frequency and the number of thermostats in the chain were fixed at  $800 \text{ cm}^{-1}$  and 7, respectively. These choices were further validated by the good agreement obtained between the MCPT and MDPT simulations on the two bare water clusters (see section 3.2). A technical problem that may arise when simulating an aggregate at a rather high temperature is evaporation. Although real, this process is not desirable as it may create spurious behaviour in the solid-liquid region of the heat capacity curves investigated here. To avoid it, we applied a rigid spherical potential centered on the cluster center of mass that we defined by  $V(r) = 0.008 * (r - r_0)^4$  (in a.u.).  $r_0$  is 5 Å for  $(\text{H}_2\text{O})_6$ , 5.5 Å for  $(\text{H}_2\text{O})_8$ , 10 Å for clusters with coronene and 15 Å for clusters with circumcoronene.

Similarly to the MDPT simulations, the MCPT simulations were performed testing the PT exchanges each 1000 MC steps. The displacement amplitudes were adapted every 50 steps to reach an average 50% acceptance. Finally, as for the MD simulations, a rigid spherical wall centered on the cluster center of mass was applied. Its radius was fixed at 5.0 and 5.5 Å for  $(\text{H}_2\text{O})_6$  and  $(\text{H}_2\text{O})_8$ , respectively. As a number of previous studies were achieved using a rigid water molecule model,<sup>61-63</sup> we also wanted to address the role of the intramolecular modes in the heat capacity curves. Thus, in the framework of the MC simulations, the heat capacity curves of the bare water clusters have been computed with and without freezing the intramolecular degrees of freedom of the water molecules.

Achieving a proper convergence of the heat capacity curves is never a straightforward task. Thus, to evaluate the convergence of our results we applied the following procedure: after removing the 10% first points of the simulation, we independently evaluated the heat capacity curve of the four quarters of the remaining data. When the four corresponding curves were found to be similar we considered the simulation as converged and we further performed a final calculation including the whole set of data but the 10% first points. In the section 1 of the Supp. Info., all these data are presented for the bare water hexamer. Over all our systems, we found that  $\sim 10^6$  single points are necessary for the equilibration of the system followed by about  $\sim 10^7$  single points to compute the heat capacity curves. As highlighted in other studies,<sup>105,106</sup> we have observed that the heat capacity curves display a far quicker convergence when the simulations start from the

lowest-energy isomer of the considered aggregate and temperatures are changed upwards from the lowest one.

All the SCC-DFTB calculations presented in this paper were performed with the deMonNano code. Furthermore, the parallel-tempering algorithm we used for both MDPT and MCPT simulations is also implemented in a development version of the deMonNano code hosted in Toulouse.<sup>107</sup>

### 3 Results and discussion

#### 3.1 Low-Energy Structures

In order to be able to discuss heat capacity curves in terms of energy level diagrams, we first looked for the most relevant low-energy isomers of all the studied systems. For  $(\text{H}_2\text{O})_6$  and  $(\text{H}_2\text{O})_8$  in gas phase and adsorbed on the coronene, these relevant structures were already identified and discussed by Simon and co-workers.<sup>86,87</sup> For the water clusters adsorbed on the circumcoronene, we performed MDPT simulations that started from configurations designed to be similar to the global minimum of the coronene system. From these simulations, we selected a tenth of structures from which we performed local geometry optimizations to obtain the lowest energy structures. Fig. 1 displays the lowest energy structures obtained for each aggregate.

We can see on Fig. 1 that, in the global minimum of each aggregate, the water cluster is located at the edge of the PAH, with the exception of the  $\text{C}_{24}\text{H}_{12}(\text{H}_2\text{O})_8$  structure. This can be related to the fact that the largest absolute atomic charges of the PAH atoms are assigned to the hydrogen atoms and edge carbon atoms. Thus, the configurations with the water cluster on the PAH edge are stabilized as they maximise the Coulomb interaction between the water slightly negative oxygen atoms pointing toward the PAH slightly positive hydrogen atoms. Table 1 reports energy differences of a selected number of low-energy structures relative to the global minimum of each aggregate. Surprisingly, we see that the adsorption on the PAHs has different effects for the water hexamer and octamer. For the octamer, the relative energies of the first isomers with respect to the *cube* are all strongly decreased. For instance, the [240000] isomer has a relative energy of  $26.7 \text{ kJ}\cdot\text{mol}^{-1}$  in the bare water octamer which falls to 9.1 and  $4.3 \text{ kJ}\cdot\text{mol}^{-1}$  when adsorbed on the coronene and circumcoronene, respectively. The opposite trend is observed for the water hexamer adsorbed on the coronene. Finally, we notice that in the case of the water hexamer adsorbed on circumcoronene, the relative energy of the *cage* structure with respect to the *prism* strongly increases whereas the opposite is observed for the *cage*, *book* and *bag* structures.

#### 3.2 Heat Capacity Curves and Phase Changes Analysis

**Water Hexamer in the Gas Phase.** In Fig. 2, we compare the heat capacity curves of  $(\text{H}_2\text{O})_6$  obtained from MDPT and MCPT simulations and, in the latter case, considering both rigid and non-rigid molecules. The two most important features of the curves discussed in the present study are the temperature of the curve's peak and the temperature of the transition's start, as obtained from a tangent crossing procedure.<sup>108</sup> The curves obtained with MDPT and non-rigid MCPT simulations are very similar with peak

Name	cycle code	$(\text{H}_2\text{O})_6$	$\text{C}_{24}\text{H}_{12}(\text{H}_2\text{O})_6$	$\text{C}_{54}\text{H}_{18}(\text{H}_2\text{O})_6$
<i>prism</i>	[2300]	0.0	0.0	0.0
<i>cage</i>	[0500]	+3.4	+13.5	+17.7
<i>book</i>	[0200]	+5.8	+7.0	+4.3
<i>bag</i>	[0120]	+7.5	+8.3	+5.5
<i>cycle</i>	[0001]	+8.9	+13.7	+7.8
Name	cycle code	$(\text{H}_2\text{O})_8$	$\text{C}_{24}\text{H}_{12}(\text{H}_2\text{O})_8$	$\text{C}_{54}\text{H}_{18}(\text{H}_2\text{O})_8$
<i>cube</i>	[060400]	0.0	0.0	0.0
	[030000]	+25.3	+11.5	+11.6
	[240000]	+26.7	+9.1	+4.3
	[111000]	+37.0	+15.6	+20.7

**Table 1** Relative SCC-DFTB energies ( $\text{kJ}\cdot\text{mol}^{-1}$ ) of selected  $(\text{H}_2\text{O})_6$  and  $(\text{H}_2\text{O})_8$  water clusters isomers in the gas phase, and adsorbed on coronene and on circumcoronene. Corresponding structures are provided in Supp. Info. (section 4).

temperatures of 88 K and 90 K, respectively, and transition starting temperatures of 57 K in both cases. The similarity of these curves suggests that we can be confident in the convergence of the simulations. It also validates the choice of the thermostat parameters used in the MDPT approach.

Performing rigid-body MCPT simulations leads to very similar results for the heat capacity curve with temperatures of 86 K for the peak maximum and 58 K for the transition beginning. This demonstrates that considering or not the intramolecular modes, at least in a classical picture, has only minor influence on the melting temperature of these aggregates, which validates the rigid-body approximation used in a number of works reported in the literature.<sup>61–64,66,67</sup>

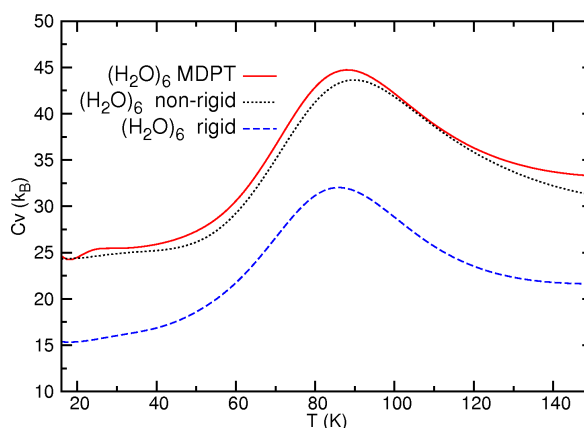


**Fig. 2** Heat capacity curves of  $(\text{H}_2\text{O})_6$  in the gas phase from MDPT and MCPT simulations with non-rigid and rigid body approximation.

As early claimed by Tharrington and Jordan,<sup>62</sup> the reported phase change for the water hexamer often starts by isomerisation processes. This can be seen for the water hexamer by studying the evolution of the populations of various isomers with the temperature, as presented on Fig. 3. Isomers not specifically represented on this picture are gathered in the curve named "others". Below  $\sim 45 \text{ K}$  only the *prism* is present. At higher temperatures, other isomers appear, successively the *inter*, *book* and *bag*. The

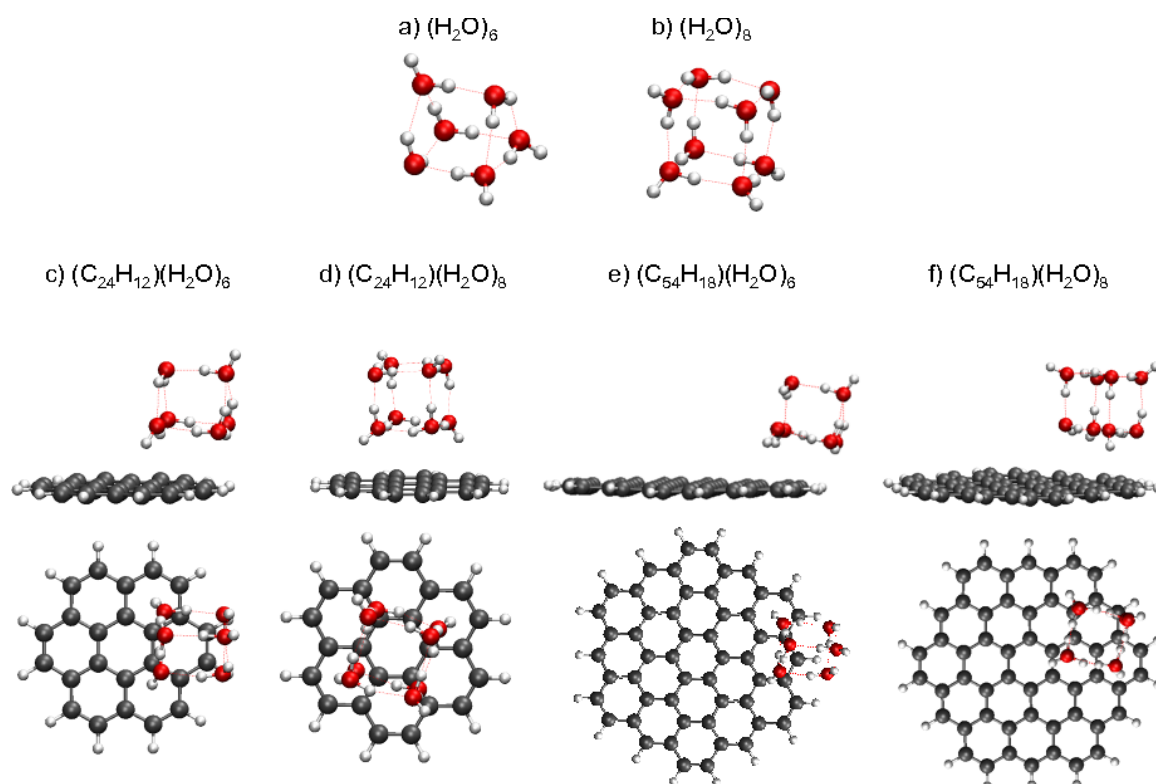


**Fig. 1** Global minima for the studied aggregates: a) Water hexamer and b) water octamer. Top and lateral views of the PAH-water cluster aggregates: c)  $C_{24}H_{12}(H_2O)_6$ , d)  $C_{24}H_{12}(H_2O)_8$ , e)  $C_{54}H_{18}(H_2O)_6$  and f)  $C_{54}H_{18}(H_2O)_8$ .

presence of these various isomers agree with the experimental evidence that even at very low temperature several isomers can be detected.<sup>50</sup> However, in contrast to these measurements, the *cage*, which is the experimental minimum energy structure, only appears at  $\sim 80$  K in our simulation. The presence of these isomers demonstrates that at temperatures higher than 45 K the aggregate has enough internal energy to visit other local minima of the PES which is the sign that a phase change is occurring. The temperature at which a significant number of isomers coexist, *i.e.*  $\sim 90$  K, agrees with the temperature of the maximum of the heat capacity curve. Fig. 3 is similar to the picture presented by Wang *et al.*<sup>51</sup> in their study of the water hexamer with the WHBB potential.<sup>109</sup> The authors also performed simulations with the path-integral molecular dynamics (PIMD) approach to take into account nuclear quantum effects (NQE) on the isomer populations. They observed a net influence of the NQE in between 30 and 90 K which supposes that their inclusion in the present simulation would lead to a shift of the heat capacity curve towards lower temperatures. This behaviour has already been observed by Asare and coworkers in their path-integral MC study of the water octamer performed using the TIP4P potential.<sup>65,110</sup> Although being a non-flexible potential, the strong shift of the heat capacity curve towards lower temperatures is expected to be transferable to other more elaborated potentials such as our SCC-DFTB one.

A number of important points can be inferred from the heat capacity curves obtained from FF potentials previously reported in the literature.<sup>61,62</sup> First, the shape of the simulated curve strongly

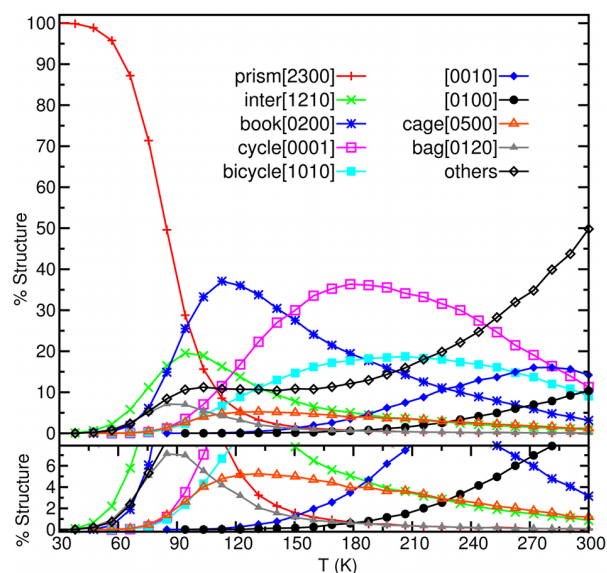


**Fig. 3** Temperature-evolution of the isomer populations of  $(H_2O)_6$  obtained from MDPT simulations. In Supp. Info. are provided a structural representation of each of these isomers (section 4.1).

depends on the energy level diagram given by a particular potential, *i.e.* potentials leading to different energy level diagrams would lead to different heat capacity curves. Second, three-site potentials such as TIP3P or SPC/E seem to perform less well than four-site potentials such as DC, MCY or even TIP4P. For example, TIP4P and TIP3P lead to maxima in the heat capacity curve of  $(\text{H}_2\text{O})_6$  at 90 and 50 K, respectively. Pedulla and Jordan analysed these discrepancies in terms of a different ordering of the lowest energy minima predicted by the potentials.<sup>61</sup> Thus, heat capacity curves are strongly sensitive to the description of the intermolecular electrostatic interaction that controls the energy level diagram of the aggregate. This sensitivity can also be highlighted in the framework of the SCC-DFTB approach if we compare the results obtained with the original Mulliken charges and the CM3 charges. The corresponding curves are provided in Supp. Info. (section 2.1) and, as expected, display strong discrepancies for both water hexamer and octamer. Simon *et al.* demonstrated that the SCC-DFTB approach modified to incorporate CM3 charges reproduces very well the energy level diagram of the water hexamer, as compared to the MP2 or CCSD(T) approaches.<sup>85</sup> Consequently, one can be confident in the accuracy of the results with respect to the present potential.

**Water Octamer in the Gas Phase.** The heat capacity curves for  $(\text{H}_2\text{O})_8$  are reported on Fig. 4. As for the hexamer, the similarity between the curves derived from MCPT and MDPT demonstrates the reproducibility of the present results and validates the choice of the MD thermostat parameters. For these curves, the beginning of the phase change occurs at 141 K (143 K) and the maximum of the curve is at 186 K (185 K) for the MDPT (MCPT) simulations. When the MCPT technique with the rigid-body approximation is used, the temperatures are only very slightly shifted toward lower values with 140 K for the beginning of phase change and 182 K for the peak maximum. This demonstrates that as well as in the case of  $(\text{H}_2\text{O})_6$ , the intramolecular modes do not play a significant role, at least in a classical picture, in tuning the melting temperature of the bare water octamer.

The curves of Fig. 4 display a much sharper peak and a higher transition temperature as compared with the hexamer ones. This is in agreement with some previous studies on this aggregate.<sup>61,62,65,110</sup> The higher peak temperature is consistent with the fact that the relative energies of typical isomers with respect to the most stable one are significantly larger for the octamer than for the hexamer (see Table 1).

The analysis of the isomer populations of the octamer presented in Fig. 5 reveals strong differences with those of the hexamer. Indeed, while in the hexamer the phase change is characterised by the gradual onset of a number of well defined isomers, in the octamer, as soon as the phase change starts, a very large number of isomers appear within a narrow range of temperatures. Thus, except for the *cube* isomer – which predominates up to  $\sim 180$  K – only one other isomer reaches 10% of presence whatever the temperature.

Choi rationalized the influence of various corrections to the original SCC-DFTB on the octamer heat capacity curves derived from MCPT simulation.<sup>64</sup> Starting from the original SCC-DFTB formulation including the dispersion correction proposed by Elst-

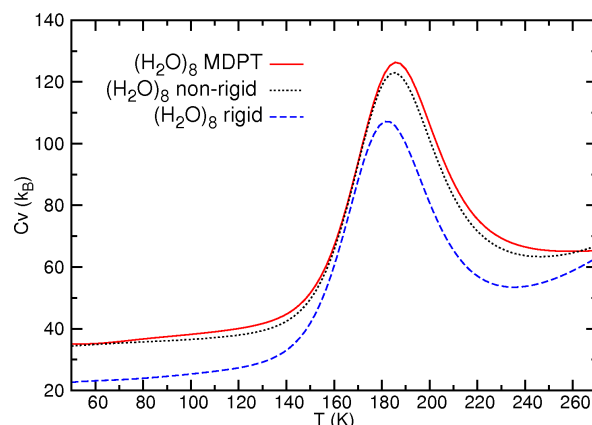


**Fig. 4** Heat capacity curves of  $(\text{H}_2\text{O})_8$  in the gas phase from MDPT and MCPT simulations with non-rigid and rigid body approximation.

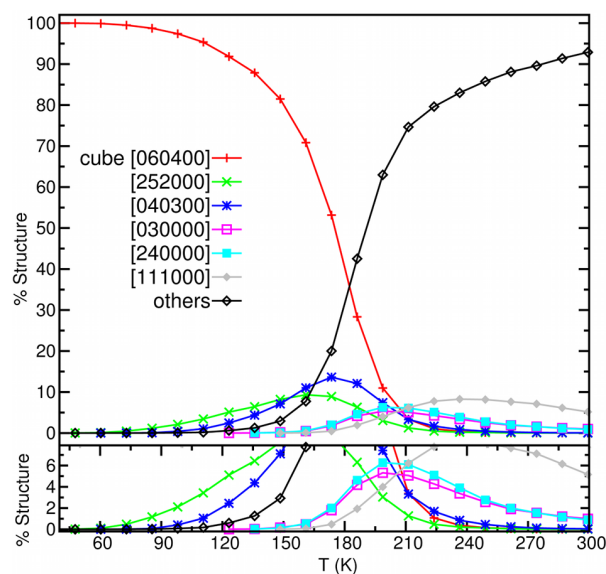


**Fig. 5** Temperature-evolution of the isomer populations of  $(\text{H}_2\text{O})_8$  obtained from MDPT simulations. In Supp. Info. (section 4.4) are provided structural representations of all isomers.

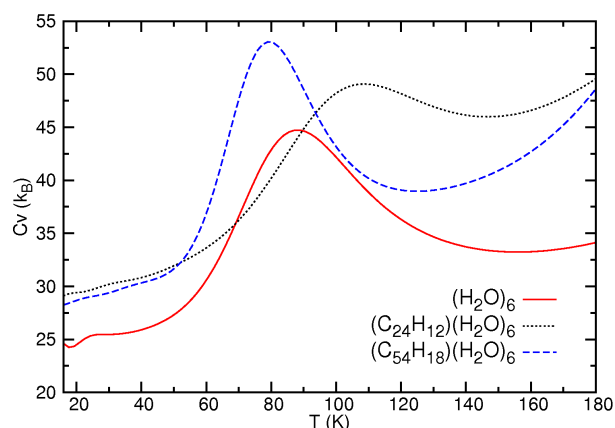


**Fig. 6** Comparison of the heat capacity curves of  $(\text{H}_2\text{O})_6$  in the gas phase and adsorbed on the coronene and on the circumcoronene (obtained from MDPT simulations).

ner *et al.*<sup>111</sup> (referred to as SCC-DFTB+D) the author included two corrections to the charges: first by modifying the  $\gamma$  function and referred to as SCC-DFTB+D[HB], second by including a third order term (DFTB3)<sup>112</sup> and referred to as SCC-DFTB+D[HB+third]. The SCC-DFTB+D method leads to a melting transition of  $\sim 134$  K whereas SCC-DFTB+D[HB] and SCC-DFTB+D[HB+third] lead to a melting temperature of  $\sim 208$  and  $\sim 212$  K, respectively. As for the water hexamer, we see that the level of treatment of the electrostatic interaction strongly influences the features of the heat capacity curve. Interestingly, the values obtained with the SCC-DFTB+D[HB] and SCC-DFTB+D[HB+third] methods are consistent with the results obtained with the CM3 charges scheme and a different dispersion correction.<sup>93–95</sup> As the energy level diagrams obtained with these three approaches are all similar to the MP2 one, the similarity of the corresponding heat capacity curves was expected. The effect of the atomic charges choice on the heat capacity curve is illustrated in Supp. Info. (section 2.2).

**Water Hexamer Adsorbed on  $\text{C}_{24}\text{H}_{12}$  and on  $\text{C}_{54}\text{H}_{18}$ .** We now discuss the case of the water hexamer adsorbed on top of two different PAHs. As shown in Fig. 6, the peak temperature is  $\sim 109$  K when  $(\text{H}_2\text{O})_6$  is adsorbed on the coronene and  $\sim 79$  K when adsorbed on the circumcoronene.

The increase of the melting temperature in the case of adsorption on coronene can be understood from the energy level diagram of the water cluster, isolated and adsorbed. As already shown by Simon and Spiegelman,<sup>86</sup> and reported in Table 1, the *prism* isomer is more stabilized by the presence of the PAH than the other low-energy isomers are. A higher temperature is then necessary to visit the latter. The distributions of isomers, shown in Fig. 7, present considerable differences with that of the corresponding isolated water cluster (Fig. 3). In particular, the populations of the *book* and *cycle* isomers decrease to values close to the ones of the *inter* isomer, that is,  $\sim 20\%$ .

The prediction of the melting temperature from the evolution of the energy of the typical isomers is much less straightforward in the case of adsorption on circumcoronene. For the most impor-

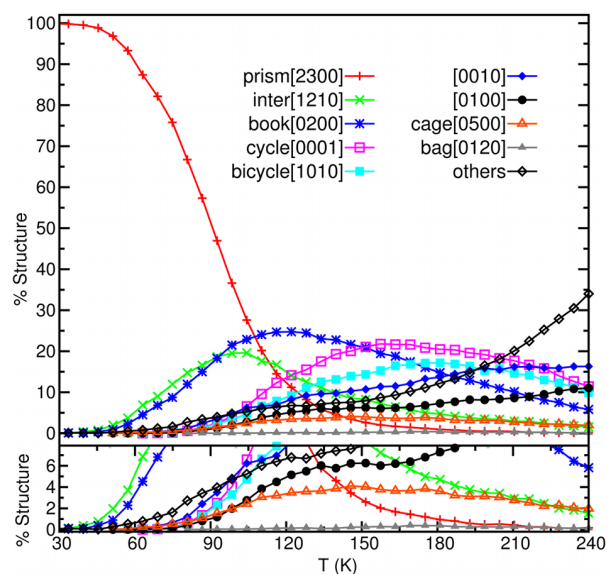


**Fig. 7** Temperature-evolution of the isomer populations of  $(\text{C}_{24}\text{H}_{12})(\text{H}_2\text{O})_6$  obtained from MDPT simulations. In Supp. Info. (section 4.2) are provided structural representations of all isomers.

tant isomers involved in the phase change of the isolated water hexamer (Fig. 3), the relative energy with respect to the *prism* increases for the *cage* structure but decreases for the *book* and *cycle* structures (see Table 1). This results in a slight decrease of the hexamer melting temperature (Fig. 6) when adsorbed on the circumcoronene, related to an abrupt appearance of the *book* and *cycle* isomers (Fig. 8). In contrast, the *inter* structure contribution declines to a value close to 6.5% whereas it reaches  $\sim 20\%$  in the isolated cluster.

In order to better understand the differences in the shifts of the heat capacity curve's peak for adsorption on coronene and on circumcoronene, we have plotted the mean distance (hereafter referred to as  $\langle d \rangle$ ) between the center of mass of the PAH and the center of mass of the water cluster projected onto the PAH plane as a function of the temperature (see Fig. 9). In the case of coronene, the water cluster at low temperatures remains above an edge cycle and  $\langle d \rangle$  decreases smoothly from  $\sim 3$  to  $\sim 2$  Å for higher temperatures. Even at temperatures between 100 and 180 K,  $\langle d \rangle$  remains around 2 Å despite strong fluctuations around this value. The situation is different for circumcoronene. At low temperatures, the hexamer cluster is also located at the edge, which is correlated with large values for  $\langle d \rangle$  up to 70 K. Above this temperature, the cluster motion undergoes quite rapid transition towards a diffusive regime. Then, the water cluster essentially moves above the second cycle crown, recovering a behavior of same mean amplitude as for coronene ( $\langle d \rangle \sim 2$  Å). This local-to-diffusive transition around 80 K is correlated with the heat capacity curve's peak (see Fig. 6). Thus, in addition to the aforementioned energetic considerations, the differences observed for the heat capacity curves for the water hexamer adsorbed on circumcoronene vs coronene can also be related to the

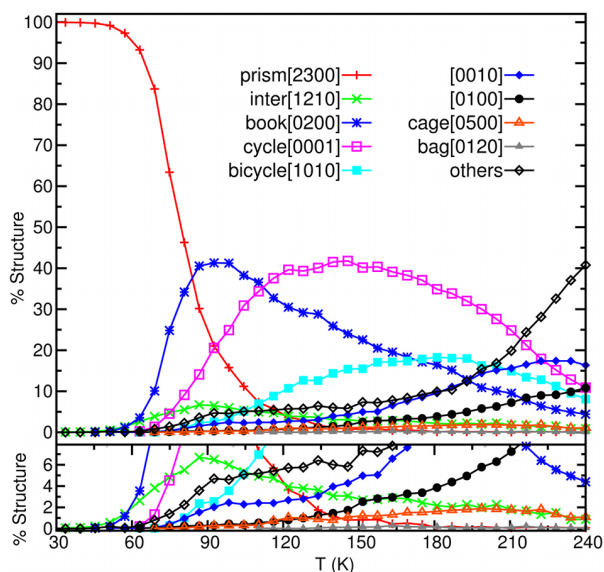


**Fig. 8** Temperature-evolution of the isomer populations of  $(C_{54}H_{18})(H_2O)_6$  obtained from MDPT simulations. In Supp. Info. (section 4.3) are provided structural representations of all isomers.

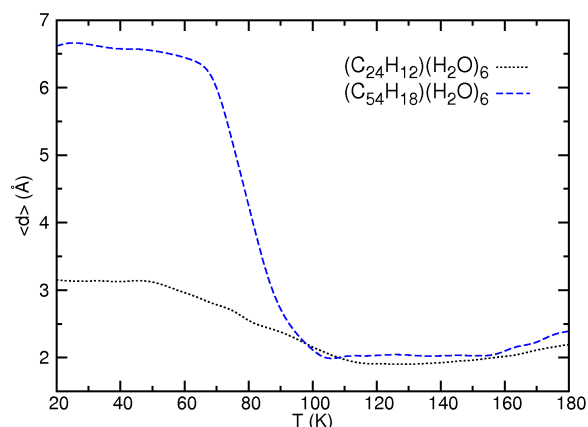


**Fig. 9** Temperature-evolution of the mean distance  $\langle d \rangle$  between the center of mass of the PAH and the center of mass of the water hexamer projected on the PAH plane.

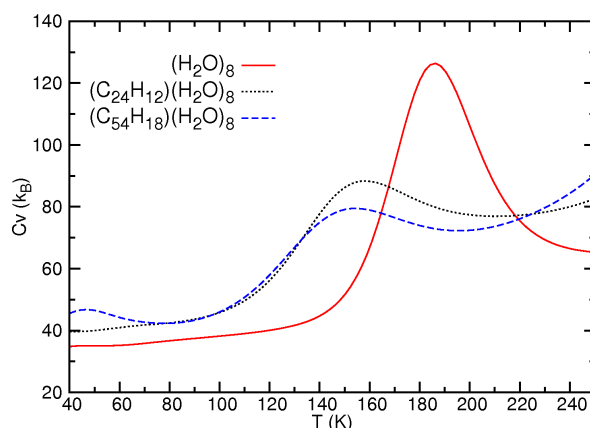


**Fig. 10** Heat capacity curves of  $(H_2O)_8$  in the gas phase, adsorbed on the coronene and adsorbed on the circumcoronene (obtained from MDPT simulations).

dynamical behavior bound to the different sizes of the PAH substrate.

**Water Octamer Adsorbed on  $C_{24}H_{12}$  and on  $C_{54}H_{18}$ .** Fig. 10 reports the heat capacity curves of the water octamer adsorbed on top of the two different PAHs. In contrast with the hexamer case, the temperature at which these curves reach their maxima are similar and about 155 K, *i.e.*  $\sim 30$  K below the position of the maximum of the bare water octamer.

This clear and similar influence of the PAHs is thus opposite to the one observed for the water hexamer. Nevertheless, its explanation can also be found in the energy level diagram of the water clusters in the gas phase and adsorbed on the PAHs, as the gap between the most stable cubic structure and the energetically higher isomers is strongly reduced when the cluster is adsorbed on the PAH surface, as shown in ref<sup>87</sup> and reported in Table 1. Interestingly, a similar evolution of the relative energy of the isomer was previously reported for the water octamer adsorbed on a cationic fullerene,  $C_{60}^+(H_2O)_8$ .<sup>66</sup> This observation was also used to interpret a phase change shift toward lower temperatures when the water octamer is adsorbed on  $C_{60}^+$ .

The analysis of the isomer populations for the water octamer-PAH aggregates is shown in Fig. 11 and Fig. 12. One of the main differences between Fig. 11, Fig. 12 and Fig. 5 is the temperature at which the *cube* represents 50% of the population. It is  $\sim 174$  K for the bare octamer against 142 K and 123 K for the cluster on coronene and circumcoronene, respectively. This shift is strongly related to the decrease of the heat capacity curves maxima. In addition, as for the hexamer, one also observes modifications of the populations of various isomers. For instance, the [040300] isomer reaches a maximum occurrence at  $\sim 13.6\%$  for the bare cluster while on both PAHs it is never higher than 7.5%. Another population that encounters significant changes is that of the [240000] isomer, almost constant and low ( $< 6.5\%$ ) for the octamer in the gas phase and adsorbed on the coronene whereas it increases up to 18.5% on the circumcoronene.

Fig. 13 reports the temperature-evolution of  $\langle d \rangle$  as previously defined. In the case of coronene, at low temperatures, the

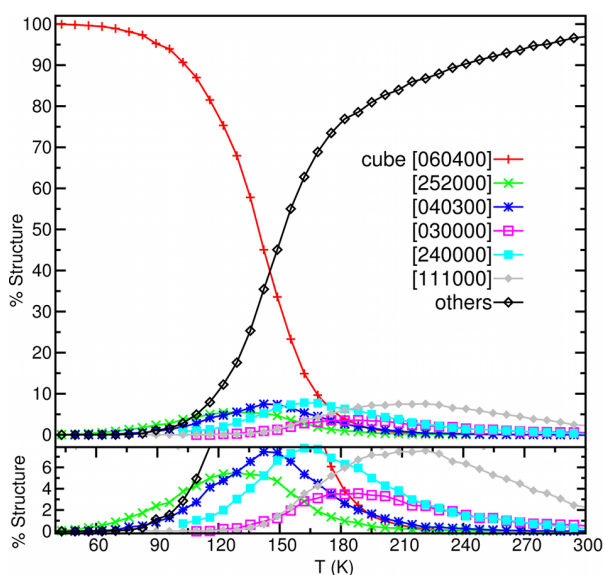


**Fig. 11** Temperature-evolution of the isomer populations of  $(C_{24}H_{12})(H_2O)_8$  obtained from MDPT simulations. In Supp. Info. (section 4.5) are provided structural representations of all isomers.

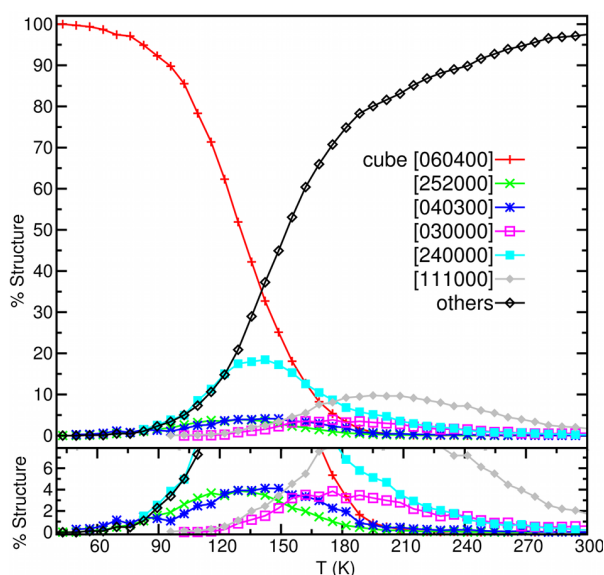


**Fig. 12** Temperature-evolution of the isomer populations of  $(C_{54}H_{18})(H_2O)_8$  obtained from MDPT simulations. In Supplementary Information (section 4.6) are provided structural representations of all isomers.

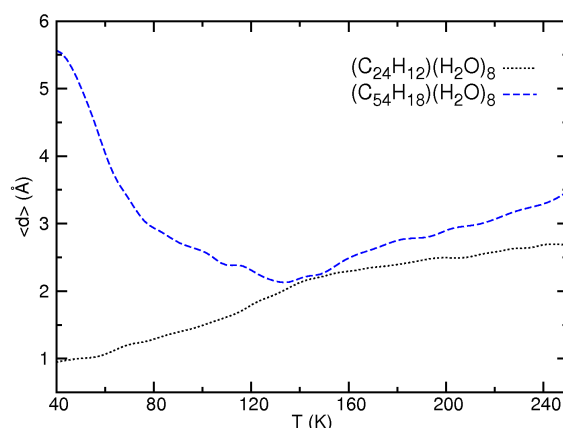


**Fig. 13** Temperature-evolution of the mean distance  $\langle d \rangle$  between the center of mass of the PAH and the center of mass of the water octamer projected on the PAH plane.

cluster remains around its lowest equilibrium structure above the central cycle ( $\sim 1$  Å) and undergoes a very smooth diffusive process. Alternatively, in the case of circumcoronene, the water cluster is located close to the edge at low temperature and undergoes diffusion over the whole PAH above 100 K. In both cases, the evolutions are much smoother than in the water hexamer-circumcoronene case. Both transitions for the octamer take place at significantly lower temperatures ( $T < 150$  K) than the isolated water octamer phase change temperature ( $\sim 185$  K). Thus, in the present case, both energetic and dynamical behaviors lead to a decrease of the characteristic phase change temperature.

We also performed simulation of the octamer adsorbed on either coronene or circumcoronene without freezing the PAH intramolecular modes. As shown in Supp. Info. (sections 3.1 and 3.2), this results in a small shift towards lower temperatures of the heat capacity curve. Consequently, our conclusions are the same whether the PAH is treated as a rigid body or not. This has important implications as it somewhat validates the results of the number of studies performed using rigid-body FFs.

## 4 Conclusions

We showed in this paper the applicability of the SCC-DFTB method in the study of thermodynamic properties for small water clusters isolated and adsorbed on PAHs. We devoted our efforts to the investigation of phase changes through the simulation of heat capacity curves. In order to explore the PES of the bare water clusters, we used MCPT, both in its standard non-rigid body formulation and using the rigid-body approximation, and MDPT approaches. We found that the three approaches lead to similar temperature of the phase changes. This endorses the majority of the studies in the literature that usually make use of the MCPT technique in the rigid-body approximation. In the case of water clusters adsorbed on PAH, the present simulations show that the temperature triggering phase changes are related to two factors. One is the energy level diagram of the considered aggregate. The second one is the dynamical behavior which depends obviously on the size and geometry of the water cluster but also on the size

of the PAH. In both water clusters, the changes are substantial and demonstrate a strong influence of the PAH on the thermodynamic properties of the water cluster. However, different trends are observed. For the water octamer, the peak temperature decreases when adsorbed on the PAHs with respect to its value in the isolated cluster, whereas for the water hexamer it depends on the PAH.

In addition to the heat capacity curves, we studied the population of the water isomers for each of the studied aggregates. This allowed us to investigate the relationship between these heat capacity behaviors and the corresponding structural transformations in the water clusters. We observed a remarkable influence of the PAH, mainly for the case of water hexamer-PAH aggregates. The temperatures at which the population of the global minima give place to a high number of other isomers systematically correspond to the temperatures of the maximum of the heat capacity curve.

This work paves the way towards phase change studies of larger water clusters using the SCC-DFTB technique. This is of major importance as a number of publications dealing with experimental measurements of heat capacity curves of large water clusters are available and no theoretical interpretation has yet been proposed. Moreover, another perspective of the present work would be to include nuclear quantum effects, for instance through the use of the path-integral molecular dynamics approach.

### Acknowledgements

This study has been supported through the NEXT grant ANR-10-LABX-0037 in the framework of the "Programme des Investissements d'Avenir". It has also been supported by ANR 13-BS08-0005 PARCS: Polycyclic Aromatic hydrocarbons Reactivity in Cryogenic Solids and GDR Groupement de Recherche 3533 EMIE Edifices Moléculaires Isolés et Environnés. The authors acknowledge the supercomputing facility of CALMIP for generous allocation of computer resources.

### References

- 1 A. Léger and J. L. Puget, *Astronom. Astrophys.*, 1984, **137**, L5–L8.
- 2 L. J. Allamandola, A. G. G. M. Tielens and J. R. Barker, *Astrophys. J. Lett.*, 1985, **290**, L25–L28.
- 3 J. L. Puget and A. Léger, *Annu. Rev. Astro. Astrophys.*, 1989, **27**, 161–198.
- 4 L. J. Allamandola, D. M. Hudgins and S. A. Sandford, *Astrophys. J. Lett.*, 1999, **511**, L115.
- 5 D. K. Bohme, S. Wlodek and H. Wingel, *J. Am. Chem. Soc.*, 1991, **113**, 6396–6041.
- 6 C. W. Bauschlicher, *Mol. Phys.*, 2009, **107**, 809–818.
- 7 Joalland, B., Simon, A., Marsden, C. J. and Joblin, C., *Astron. Astrophys.*, 2009, **494**, 969–976.
- 8 B. Joalland, M. Rapacioli, A. Simon, C. Joblin, C. J. Marsden and F. Spiegelman, *J. Phys. Chem. A*, 2010, **114**, 5846–5854.
- 9 A. Simon and C. Joblin, *J. Phys. Chem. A*, 2007, **111**, 9745–9755.
- 10 A. Simon and C. Joblin, *Astrophys. J.*, 2010, **712**, 69–77.
- 11 C. Joblin, J. Maillard, I. Vauglin, C. Pech and P. Boissel, *Probing the connection between PAHs and hydrogen (H, H<sub>2</sub>) in the laboratory and in the interstellar medium*, ed McGraw-Hill, ed. F. Combes and G.P. DesForets, 2000, pp. 107–114.
- 12 E. Rauls and L. Hornekær, *Astrophys. J.*, 2008, **679**, 531.
- 13 W. A. Schutte, A. G. G. M. Tielens and L. Allamandola, *Astrophys. J.*, 1993, **415**, 397–414.
- 14 V. L. Page, T. P. Snow and V. M. Bierbaum, *Astrophys. J.*, 2003, **584**, 316.
- 15 S. O. Baek, R. a. Field, M. E. Goldstone, P. W. Kirk, J. N. Lester and R. Perry, *Water Air Soil Pollut*, 1991, **60**, 279–300.
- 16 B. Finlayson-Pitts and J. Pitts, *Atmospheric Chemistry, Fundamental and Experimental Techniques*, Wiley-Vch Verlag Berlin GmbH, 1986.
- 17 D. Phillips, *Nature*, 1983, **303**, 468–472.
- 18 T. M. Penning, M. E. Burczynski, C.-f. Hung, K. D. Mccoull, N. T. Palackal and L. S. Tsuruda, *Chem. Res. Toxicol.*, 1999, **12**, 1–18.
- 19 M. M. Pratt, K. John, A. B. MacLean, S. Afework, D. H. Phillips and M. C. Poirier, *Int. J. Environ. Res. Publ. Health.*, 2011, **8**, 2675–91.
- 20 C.-T. Li, H.-K. Zhuang, L.-T. Hsieh, W.-J. Lee and M.-C. Tsao, *Environ. Int.*, 2001, **27**, 61 – 67.
- 21 S. Wu, S. Tao, F. Xu, R. Dawson, T. Lan, B. Li and J. Cao, *Sci. Total Environ.*, 2005, **345**, 115 – 126.
- 22 M. Blanchard, M.-J. Teil, E. Guigon, K. Larcher-Tiphagne, D. Ollivon, B. Garban and M. Chevreuil, *Sci. Total Environ.*, 2007, **375**, 232 – 243.
- 23 A. Birgül, Y. Tasdemir and S. S. Cindoruk, *Atmos. Res.*, 2011, **101**, 341 – 353.
- 24 A. D. P. Netto, T. M. Krauss, I. F. Cunha and E. C. Rego, *Water Air Soil Pollut*, 2006, **176**, 57–67.
- 25 S. D. Dalosto and S. Tinte, *J. Phys. Chem. C*, 2011, **115**, 4381–4386.
- 26 D. J. Cole, P. K. Ang and K. P. Loh, *J. Phys. Chem. Lett.*, 2011, **2**, 1799–1803.
- 27 K. Falk, F. Sedlmeier, L. Joly, R. R. Netz and L. Bocquet, *Nano Lett.*, 2010, **10**, 4067–73.
- 28 M. Pumera, *Chem. Soc. Rev.*, 2010, **4**, 4146–4157.
- 29 D. Cohen-Tanugi and J. C. Grossman, *Nano Lett.*, 2012, **12**, 3602–8.
- 30 A. Nilsson and L. Pettersson, *Chem. Phys.*, 2011, **389**, 1 – 34.
- 31 A. Vitek, D. J. Arismendi-Arrieta, R. Rodriguez-Cantano, R. Prosmiiti, P. Villarreal, R. Kalus and G. Delgado-Barrio, *Phys. Chem. Chem. Phys.*, 2015, **17**, 8792–8801.
- 32 D. J. Wales and M. P. Hodges, *Chem. Phys. Lett.*, 1998, **286**, 65–72.
- 33 D. J. Wales, *Energy Landscapes with Applications to Clusters, Biomolecules and Glasses*, Cambridge University Press, 2003.
- 34 J. Hernández-Rojas and D. J. Wales, *Chemical Physics*, 2014, **444**, 23–29.
- 35 H. Takeuchi, *J. Chem. Inf. Model.*, 2008, **48**, 2226–2233.

- 36 G. A. Tribello, J. Cuny, H. Eshet and M. Parrinello, *J. Chem. Phys.*, 2011, **135**, 114109.
- 37 J. L. Llanio-Trujillo, J. M. C. Marques and F. B. Pereira, *J. Phys. Chem. A*, 2011, **115**, 2130–2138.
- 38 K. Liu, M. G. Brown, C. Carter, R. J. Saykally, J. K. Gregory and D. C. Clary, *Nature*, 1996, **381**, 501–503.
- 39 K. Liu, M. G. Brown and R. J. Saykally, *J. Phys. Chem. A*, 1997, **101**, 8995–9010.
- 40 F. N. Keutsch and R. J. Saykally, *Proc. Natl. Acad. Sci. U.S.A.*, 2001, **98**, 10533–10540.
- 41 M. Losada and S. Leutwyler, *J. Chem. Phys.*, 2002, **117**, 2003–2016.
- 42 M. Losada and S. Leutwyler, *J. Chem. Phys.*, 2003, **119**, 304–312.
- 43 C. Steinbach, P. Andersson, M. Melzer, J. K. Kazimirski, U. Buck and V. Buch, *Phys. Chem. Chem. Phys.*, 2004, **6**, 3320–3324.
- 44 B. Santra, A. Michaelides, M. Fuchs, A. Tkatchenko, C. Filippi and M. Scheffler, *J. Chem. Phys.*, 2008, **129**, 194111.
- 45 A. K. Kelkkanen, B. I. Lundqvist and J. K. Nørskov, *J. Chem. Phys.*, 2009, **131**, 046102.
- 46 P. L. Silvestrelli, *Chem. Phys. Lett.*, 2009, **475**, 285–288.
- 47 D. M. Bates and G. S. Tschumper, *J. Phys. Chem. A*, 2009, **113**, 3555–9.
- 48 R. J. Saykally and D. J. Wales, *Science*, 2012, **336**, 814–815.
- 49 J. Ceponkus, P. Uvdal and B. Nelander, *J. Phys. Chem. A*, 2012, **116**, 4842–4850.
- 50 C. Perez, M. T. Muckle, D. P. Zaleski, N. A. Seifert, B. Temelso, G. C. Shields, Z. Kisiel and B. H. Pate, *Science*, 2012, **336**, 897–901.
- 51 Y. Wang, V. Babin, J. M. Bowman and F. Paesani, *J. Am. Chem. Soc.*, 2012, **134**, 11116–11119.
- 52 K. Kim, M. Dupuis, G. Lie and E. Clementi, *Chem. Phys. Lett.*, 1986, **131**, 451–456.
- 53 C. J. Tsai and K. D. Jordan, *J. Chem. Phys.*, 1991, **95**, 3850.
- 54 K. Laasonen, M. Parrinello, R. Car, C. Lee and D. Vanderbilt, *Chemical Physics Letters*, 1993, **207**, 208–213.
- 55 J. Kim, B. J. Mhin, S. J. Lee and K. S. Kim, *Chem. Phys. Lett.*, 1994, **219**, 243–246.
- 56 J. O. Jensen, P. N. Krishnan and L. A. Burke, *Chem. Phys. Lett.*, 1995, **246**, 13–19.
- 57 E. S. Kryachko, *Int. J. Quant. Chem.*, 1998, **70**, 831–853.
- 58 S. Maheshwary, N. Patel, N. Sathyamurthy, A. D. Kulkarni and S. R. Gadre, *J. Phys. Chem. A*, 2001, **105**, 10525–10537.
- 59 U. Buck, I. Ettischer, M. Melzer, V. Buch and J. Sadlej, *Phys. Rev. Lett.*, 1998, **80**, 2578–2581.
- 60 C. J. Gruenloh, J. R. Carney, C. A. Arrington, T. S. Zwier, S. Y. Fredericks and K. D. Jordan, *Science*, 1997, **276**, 1678–1681.
- 61 J. M. Pedulla and K. D. Jordan, *Chem. Phys.*, 1998, **239**, 593–601.
- 62 A. N. Tharrington and K. D. Jordan, *J. Phys. Chem. A*, 2003, **107**, 7380–7389.
- 63 J. Douady, F. Calvo and F. Spiegelman, *Eur. Phys. J. D*, 2009, **52**, 47–50.
- 64 T. H. Choi, *Chem. Phys. Lett.*, 2012, **543**, 45–49.
- 65 E. Asare, A.-R. Musah, E. Curotto, D. L. Freeman and J. D. Doll, *J. Chem. Phys.*, 2009, **131**, 184508–11.
- 66 J. Hernández-Rojas, F. Calvo, F. Rabilloud, J. Bretón and J. M. Gomez Llorente, *J. Phys. Chem. A*, 2010, **114**, 7267–74.
- 67 J. Hernández-Rojas, F. Calvo, J. Breto and J. M. G. Llorente, *J. Phys. Chem. C*, 2012, **116**, 17019–17028.
- 68 W. L. Jorgensen, J. Chandrasekhar, J. D. Madura, R. W. Impey and M. L. Klein, *J. Chem. Phys.*, 1983, **79**, 926–935.
- 69 W. L. Jorgensen and J. Tirado-Rives, *J. Am. Chem. Soc.*, 1988, **110**, 1657–1666.
- 70 H. J. C. Berendsen, J. R. Grigera and T. P. Straatsma, *J. Phys. Chem.*, 1987, **91**, 6269–6271.
- 71 O. Matsuoka, E. Clementi and M. Yoshimine, *J. Chem. Phys.*, 1976, **64**, 1351–1361.
- 72 P. Cieplak, P. Kollman and T. Lybrand, *J. Chem. Phys.*, 1990, **92**, 6755–6760.
- 73 U. Niesar, G. Corongiu, E. Clementi, G. R. Kneller and D. K. Bhattacharya, *J. Phys. Chem.*, 1990, **94**, 7949–7956.
- 74 L. X. Dang, *J. Chem. Phys.*, 1992, **97**, 2659–2660.
- 75 L. X. Dang and T.-M. Chang, *J. Chem. Phys.*, 1997, **106**, 8149–8159.
- 76 D. N. Bernardo, Y. Ding, K. Krogh-Jespersen and R. M. Levy, *J. Phys. Chem.*, 1994, **98**, 4180–4187.
- 77 W. M. C. Foulkes and R. Haydock, *Phys. Rev. B*, 1989, **39**, 12520–12536.
- 78 D. Porezag, T. Frauenheim, T. Köhler, G. Seifert and R. Kaschner, *Phys. Rev. B*, 1995, **51**, 12947–12957.
- 79 D. Porezag, T. Frauenheim, T. Köhler, G. Seifert and R. Kaschner, *Phys. Rev. B*, 1995, **51**, 12947–12957.
- 80 M. Elstner, D. Porezag, G. Jungnickel, J. Elsner, M. Haugk, T. Frauenheim, S. Suhai and G. Seifert, *Phys. Rev. B*, 1998, **58**, 7260–7268.
- 81 M. Rapacioli, F. Spiegelman, D. Talbi, T. Mineva, A. Goursot, T. Heine and G. Seifert, *J. Chem. Phys.*, 2009, **130**, 244304–244310.
- 82 M. Rapacioli, F. Spiegelman, A. Scemama and A. Mirtschink, *J. Chem. Theory Comput.*, 2011, **7**, 44–55.
- 83 M. Rapacioli, A. Simon, L. Dontot and F. Spiegelman, *Phys. Stat. Solidi B*, 2012, **249**, 245–258.
- 84 A. Simon, M. Rapacioli, M. Lanza, B. Joalland and F. Spiegelman, *Phys. Chem. Chem. Phys.*, 2011, **13**, 3359–74.
- 85 A. Simon, M. Rapacioli, J. Mascetti and F. Spiegelman, *Phys. Chem. Chem. Phys.*, 2012, 6771–6786.
- 86 A. Simon and F. Spiegelman, *J. Chem. Phys.*, 2013, **138**, 194309.
- 87 A. Simon and F. Spiegelman, *Comp. Theor. Chem.*, 2013, **1021**, 54–61.
- 88 P. Goyal, H.-J. Qian, S. Irle, X. Lu, D. Roston, T. Mori, M. Elstner and Q. Cui, *J. Phys. Chem. B*, 2014, **118**, 11007–11027.
- 89 P. Labastie and R. L. Whetten, *Phys. Rev. Lett.*, 1990, **65**,

- 1567–1570.
- 90 A. M. Ferrenberg and R. H. Swendsen, *Phys. Rev. Lett.*, 1989, **6**, 1195–1198.
- 91 C. Bichara, J. Gaspard and J. Mathieu, *J. Chem. Phys.*, 1988, **89**, 4339–4345.
- 92 X. Yuan and A. N. Cormack, *Comput. Mater. Sci.*, 2002, **24**, 343–360.
- 93 M. Elstner, *Theor. Chem. Acc.*, 2006, **116**, 316–325.
- 94 J. Li, T. Zhu, C. Cramer and D. Truhlar, *J. Phys. Chem. A*, 1998, **102**, 1820–1831.
- 95 J. D. Thompson, C. J. Cramer and D. G. Truhlar, *J. Comput. Chem.*, 2003, **24**, 1291–1304.
- 96 M. Rapacioli, F. Spiegelman, D. Talbi, T. Mineva, A. Goursot, T. Heine and G. Seifert, *J. Chem. Phys.*, 2009, **130**, 244304–10.
- 97 Y. Sugita and Y. Okamoto, *Chem. Phys. Lett.*, 1999, **314**, 141–151.
- 98 Y. Sugita and Y. Okamoto, *Chem. Phys. Lett.*, 2000, **329**, 261–270.
- 99 U. H. E. Hansmann, *Chem. Phys. Lett.*, 1997, **281**, 140–150.
- 100 F. Calvo, *J. Chem. Phys.*, 2005, **123**, 124106–7.
- 101 G. Gamboa U., J. Vázquez-Pérez M., P. Calaminici and A. M. Köster, *Int. J. Quantum Chem.*, 2010, **110**, 2172–2178.
- 102 S. Nosé, *J. Chem. Phys.*, 1984, **81**, 511.
- 103 W. G. Hoover, *Phys. Rev. A*, 1985, **31**, 1695–1697.
- 104 M. Tuckerman, R. April, G. J. Martyna and M. L. Klein, *J. Chem. Phys.*, 1992, **97**, 2635–2644.
- 105 R. Poteau, F. Spiegelmann and P. Labastie, *Z. Phys. D*, 1994, **68**, 57–68.
- 106 F. Calvo and P. Labastie, *Eur. J. Phys.*, 2005, **26**, S23–S30.
- 107 T. Heine, M. Rapacioli, S. Patchkovskii, J. Cuny, J. Frenzel, A. Koster, P. Calaminici, H. A. Duarte, S. Escalante, R. Flores-Moreno, A. Goursot, J. Reveles, D. Salahub and A. Vela, de-MonNano, <http://demon-nano.ups-tlse.fr/>.
- 108 J. Boulon, I. Braud, S. Zamith, P. Labastie and J.-M. L'Hermite, *J. Chem. Phys.*, 2014, **140**, 164305.
- 109 Y. Wang, X. Huang, B. C. Shepler, B. J. Braams and J. M. Bowman, *J. Chem. Phys.*, 2011, **134**, 094509.
- 110 S. F. Langley, E. Curotto, D. L. Freeman and J. D. Doll, *J. Chem. Phys.*, 2007, **126**, 084506.
- 111 M. Elstner, P. Hobza, T. Frauenheim, S. Suhai and E. Kaxiras, *J. Chem. Phys.*, 2001, **114**, 5149–5155.
- 112 Y. Yang, H. Yu, D. Uork, Q. Cui and M. Elstner, *J. Phys. Chem. A*, 2007, **111**, 10861–10873.